Fuel 422 (2026) 139083

Contents lists available at ScienceDirect

Fuel

journal homepage: www.elsevier.com/locate/jfue

Full length article

Influence of Al as an alloying element on the combustion process of micron-sized iron particles

Z. Bruyr[a,*], L. Ahmad[a], L. Choisez[a], F. Halter[b], F. Contino[a]

[a] Institute of Mechanics, Materials and Civil Engineering (iMMC), Université catholique de Louvain (UCLouvain), Place du Levant, 2, 1348, Louvain-la-Neuve, Belgium
[b] CNRS – ICARE, University Orléans, Avenue de la Recherche Scientifique, 45071 Cedex 2, Orléans, France

HIGHLIGHTS

- Fe-Al powders feature more difficult ignition due to the creation of an Al-rich oxide layer.
- An Al-rich oxide lobe creates at the beginning of liquid-state combustion followed by surface oxidation.
- Evaporation is enhanced compared to pure Fe, especially for higher initial Al content.
- Full liquid-state oxidation (magnetite) is reached by ignited particles.

ARTICLE INFO

Keywords:
Renewable metal fuels
Energy storage
Iron
Aluminum
Single-particle
Alloys

ABSTRACT

While iron powder has been identified as a promising sustainable energy carrier, the influence of alloying elements on the combustion process is still not well understood. In particular, even though pure Al combustion has been extensively studied, the influence of Al as an alloying element has never been investigated before. The objective of this work is to understand how the presence of Al at varying concentrations impacts the combustion regime of Fe particles. Therefore, we produced and burned three Fe-Al powders with varying Al contents (5, 9, and 20 wt.%), using both single-particle and multi-particle combustion setups, allowing for both *in situ* visualization and *ex situ* microstructural analysis. In the multi-particle burner, the combustion products showed a limited combustion efficiency (1%) when increasing the initial Al content to 9 and 20 wt.%, compared to 86.5% for 5 wt.% initial Al content. Microstructural analysis of non-ignited particles revealed the presence of an Al_2O_3 layer, suggesting hindering internal diffusion. In the single-particle burner, particles successfully ignited and exhibited liquid-phase combustion with complex oxidation behavior, including oxide lobe formation, heterogeneous surface oxidation, and jetting and spinning behavior due to asymmetric evaporation-driven flows. Despite their low combustion efficiency, post-combustion microstructure analysis of Fe-9Al and Fe-20Al powders revealed that ignited particles fully oxidize in the liquid state and are constituted of a bi-phasic dendritic structure with Al-enriched and Fe-enriched dendrites. While combusted Fe-5Al particles are constituted of a homogeneous magnetite phase containing Al in solid solution. This study highlights the importance of Al alloying content on the combustion behavior of micron-sized Fe particles, in particular on their combustion efficiency, evaporation dynamics, or the microstructural and chemical distribution of the combustion products.

1. Introduction

Metals have recently emerged as promising carbon-free energy carriers [1]. Among them, iron powder stands out due to its high energy density, low cost, and abundance. It also presents safe and simple storage and transportation. Moreover, its combustion products are recyclable, enabling the Metal-enabled Cycle of Renewable Energy (MeCRE) [1,2].

While the combustion of pure iron powder is the primary focus of the growing research community, more economically viable iron-rich feedstocks, such as recycled steelmaking waste, could offer attractive alternatives. However, these sources are made of alloys that typically contain up to 3 wt.% of metallic impurities [3], which are difficult and costly to remove. A common metallic impurity found in low-cost steels is aluminum [3].

* Corresponding author.
Email address: zakarie.bruyr@uclouvain.be (Z. Bruyr).

https://doi.org/10.1016/j.fuel.2026.139083
Received 16 December 2025; Received in revised form 20 February 2026; Accepted 6 March 2026

Impurities significantly influence the combustion behavior of iron particles. An experimental study [4] showed that 6 wt.% Si induces a multi-peak luminosity profile, likely due to the formation of a SiO_2 layer that limits internal diffusion. Recycled mill scale containing 1.5 wt.% Mn, Al, and Si oxides exhibited slightly lower combustion efficiency than pure Fe (89–96% vs. 95–97%) but still sustained a stable flame [5,6]. Mill-scale combustion involved complex evaporation, forming mixed Cu–Ni–Mn–Fe oxide nanoparticles with traces of Mg and Ca, as well as separate Si and Cr oxides [6]. Numerical simulations further showed that up to 20 wt.% Al_2O_3, SiO_2, MnO, or CaO can reduce peak temperature without altering total energy release, although ternary oxide formation may hinder complete oxidation and reduction [7]. Experiments on direct reduced iron containing up to 2.4 wt.% oxides revealed that Al and Si increase oxygen solubility in the liquid phase and delay its release until final solidification, after magnetite dendrite formation [8]. Impurity composition also affects micro-explosion behavior, influencing internal gas generation and burst resistance [9,10].

Micron-sized iron powders undergo heterogeneous combustion [1], igniting in the solid state at a critical temperature around 1080 K [11]. Combustion then proceeds in the liquid state, with temperatures rising to 2300–2800 K [12–14], below both the boiling point of iron (3130 K) and the dissociation temperature of liquid iron oxide (3650 K). However, iron partially evaporates, forming nanoparticles, with up to 7.4 wt.% mass loss [15–17]. Peak temperature is followed by reactive cooling to solidification [12]. During liquid-phase combustion, oxidation can be limited by (I) oxygen diffusion to the particle surface, (II) surface chemisorption, and (III) internal ion diffusion [18–21]. While the exact rate-limiting steps remain under investigation, studies suggest an initial external-diffusion-limited regime influenced by surface chemisorption, transitioning to a mixed regime where internal diffusion dominates near the peak temperature and during cooling [18–21].

The combustion of pure aluminum has been widely studied for applications in solid rockets, propellants [22,23], and as a recyclable metal energy carrier [1]. While Fe-Al alloys have been examined only for combustion synthesis [24] or Al-based propellants [25,26], the liquid-phase air combustion of micron-sized Fe-Al particles remains unexplored. According to the Glassman criterion [27], micron-sized aluminum burns in air via a diffusion flame [28], with aluminum evaporating from the droplet surface and reacting with surrounding oxygen through a sequence of gas-phase reactions, ultimately yielding aluminum oxide (Al_2O_3) as the primary combustion product [29,30]. Alumina, unstable in the vapor phase, condenses into nanoparticles, forming so-called oxide smoke [31], which either disperses or redeposits on the particle, forming a distinctive cap- or lobe-shaped structure [32]. This lobe develops from the native oxide layer, which melts during ignition, and is subsequently maintained throughout liquid-phase combustion by the continuous redeposition of condensed alumina onto the surface. It reduces the effective evaporation area, prolonging burn time, and modifies local flow: Stefan flow occurs on uncovered surfaces but is absent under the lobe, generating asymmetries that can spin the particle or induce jetting [33]. Lobe growth is reinforced by phoretic effects, particularly thermophoresis and diffusiophoresis, which return nanoparticles to hot particle-bound regions adjacent to the lobe [34]. After complete aluminum consumption, the lobe solidifies into alumina, often comparable in size to the original particle. Despite extensive study, the mechanisms controlling nucleation, growth, and evolution of the alumina lobe remain incompletely understood.

The goal of this research is to understand how the presence of Al influences the combustion behavior of iron particles. Therefore, three iron-based powders with a varying Al content (5, 9, and 20 wt.%) were produced and burned, both at a single- and multi-particle scale. Laser-ignited single-particle experiments first allow to investigate the combustion behavior by *in situ* high speed imaging. Then, multi-particle combustion tests are performed in an open propane flame and post-process analysis are conducted on the collected combustion products, including microstructural and chemical characterization of the combusted products by *ex situ* x-ray diffraction (XRD), scanning electron microscopy (SEM) and energy dispersive spectroscopy (EDS). Studying the role of Al as an alloying element using this double approach represents a key novel contribution to highlight and understand its impact on ignition dynamics, on the coupled Fe-Al oxidation mechanism, and on the evolution of the phase microstructure throughout the combustion process. This enables to eventually evaluate the feasibility and key conditions to use Fe–Al alloys as a tunable class of metal fuels, but also to pave the way for other studies about the use of iron-based alloys in the MeCRE.

2. Methods

2.1. Materials and characterization methods

Three powders constituted of particles of several dozen μm diameter and with a varying Al content between 5 and 20 wt.% were produced at UClouvain using AMAZEMET ultrasonic atomization in Ar atmosphere, with a current of 120 A and a vibration frequency of 40 Hz. They are referred to as: Fe-5Al, Fe-9Al, and Fe-20Al. While typical low-cost steels and steel scraps contain up to 3 wt.% Al [3], an initial Al content of 5 wt.% was chosen to include all concerned impure Fe-Al sources. Then, to overemphasize the influence of Al, two higher Al contents were chosen that were sufficiently distinct to reveal trends and contained enough Al to amplify its effect compared with pure Fe particles. Their composition measured using Inductively Coupled Plasma (ICP) and carbon and sulfur combustion measurements is listed in Table 1. The uncertainty in the composition is 3% (relative to the measured composition) for elements present in quantities greater than 1 wt.% and ±0.01 wt.% for other elements. Unexpected Mo dissolution from the Mo vibrating plate of the ultrasonic atomizer resulted in inhomogeneous Mo intake among the atomized particles. This element was already present (~ 3 wt.%) inside Fe particles produced for our previous study [35], where we showed that they followed similar combustion as pure Fe particles.

The chemical homogeneity within a particle and in-between the particles was analyzed using Energy Dispersive X-ray Spectroscopy (EDS). Although the chemical composition is homogeneous at the particle level (see Supplementary information SI1), variations in chemical composition still exist from one particle to another within the same sample. Therefore, the dispersion in composition of each powder was statistically measured on 100 particles from each sample. The measurements indicate that the Al content may significantly vary between individual particles from the same powder, as illustrated by the median and interquartile distance of 5.1 wt.% and 3.3 wt.% for Fe-5Al (10th percentile = 2.8 wt.%; 90th percentile = 7.2 wt.%), 9.3 wt.% and 1.7 wt.% for Fe-9Al (10th percentile = 5.1 wt.%; 90th percentile = 12.2 wt.%), and 22.3 wt.% and 5.8 wt.% for Fe-20Al powder (10th percentile = 17 wt.%; 90th percentile = 25.5 wt.%). The complete statistical analysis is presented in Supplementary information SI2.

The thickness and composition of the native oxide layer were characterized using X-ray Photoelectron Spectroscopy (XPS) for each composition. The results indicate that the native oxide layer presents a thickness below the XPS probing depth of 5 to 10 nm for all Fe-Al powders (see Supplementary information SI3). The proportion of Al oxide within the oxide layer slightly increases with the Al content inside the powder (from around 20% for Fe-5Al, to 22% for Fe-9Al, and 23.4% for Fe-20Al).

Table 1
Initial powders composition in weight percent measured by ICP and carbon and sulfur combustion measurements.

[wt.%]	Fe	Al	Mo	Ti	Cu	C	S	O
Fe-5Al	95	4.5	0.4	0.04	0.01	0.01	<0.02	Bal.
Fe-9Al	89.9	9.04	0.47	–	0.01	0.02	<0.02	Bal.
Fe-20Al	76.3	19.9	3.34	–	<0.01	0.02	<0.02	Bal.

In the single-particle levitator, sieved particles with a size between 63 and 106 μm were used, as smaller particles are more difficult to position and stabilize at the center of the combustion chamber. While in the multi-particle burner, particles with a size between 45 and 63 μm were used, as this size range provided better flowability (see the particle size distribution in Fig. 1). The particle size distribution and shape parameters were measured using a Series 5000 Sync Particle Size and Shape Analysis System (Microtrac). The microstructure and local chemistry of the powders were characterized using scanning electron microscopy (SEM) ZEISS FEGSEM Ultra 55 coupled with energy-dispersive X-ray spectroscopy (EDS) before and after combustion. The powders were previously embedded in carbon-rich resin and polished through their cross-section. Phase distribution was evaluated by X-ray diffraction (XRD) using a D8 Advance from Bruker with Linxeye detector, equipped with a cobalt target operating at 30 kV and 30 mA. Before analysis, the powders were crushed to ensure the X-ray penetration depth was sufficient. The diffraction data were processed using Bruker TOPAS v.5.0 software with Rietveld refinement to identify and quantify the crystalline phases.

2.2. Single-particle levitator

The single-particle electrodynamic levitator used in this work has been extensively described in previous publications [31,35,36] to which the reader should refer for a more complete description. Particles are first charged by friction in a syringe and then suspended in the combustion chamber using electrostatic forces produced with both DC and AC electrodes (see Fig. 2). The DC electrodes are manually adjusted before each combustion test, depending on the levitating particles, with a voltage between 0 V and −1000 V for the negative electrode and between 0 V and + 1000 V for the positive one. The voltage of the AC electrode varies with time between 0 and 4000 V. Particles are then ignited symmetrically on both sides with a 50 W CO_2 infrared laser. The latter generates a Gaussian beam of 3.5 mm diameter that is split in two using a beam splitter, and then each ray is reflected by a set of mirrors to be focused on the levitating particle. Due to its temperature increase, the charged metal particle rapidly (< 0.1 ms) loses its charge [37]. Then, it allows the particles to burn autonomously from a controlled location, in a uniform gas temperature and composition field at ambient conditions (1.01 bar, 293 K and 21% O), and with a low slip velocity.

The combustion of the ignited particle is observed using a high-speed color camera PHANTOM T-2410, whose frequency is 25 kHz, exposure time is 39 μs, and with a magnification of around 1.5 μm/pixel, and a teleobjective QUESTAR QM 100. The field of view of the camera is a square of 767x767 pixels. Surface phenomena are visible due to the difference in surface emissivity between metallic and oxide liquid phases both for Fe (around 0.3 for liquid Fe and 0.7 for liquid iron oxide [39]) and Al (around 0.2 for liquid Al and between 0.4 and 0.6 for liquid alumina, computed using Mie theory as described in [31] based on the index of refraction respectively from [40–43]). The higher variation of the emissivity for liquid alumina comes from its higher variation with temperature. In addition, as the presence of Al may considerably impact the evaporation dynamics, we put a specific attention to observing the potential existence of a nanoparticles cloud and the potential particles displacement associated with evaporation flows. To enhance clarity and facilitate visualization of the surface phenomena, the background was removed from recorded snapshots using a 60% luminosity threshold from the peak luminosity to delimitate the particles boundaries. Such value was chosen based on the methodology used in our previous work to measure the particle size with a low uncertainty of 1 pixel (< 2 μm) [35].

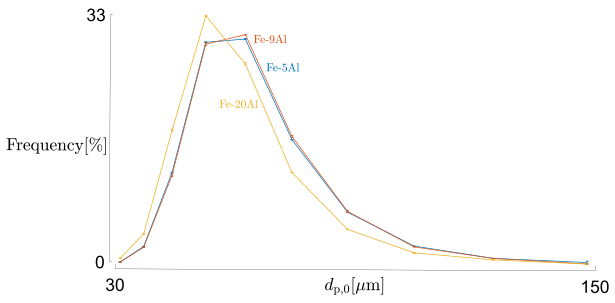

Fig. 1. Particle size distribution of the initial powders burned in the multi-particle burner.

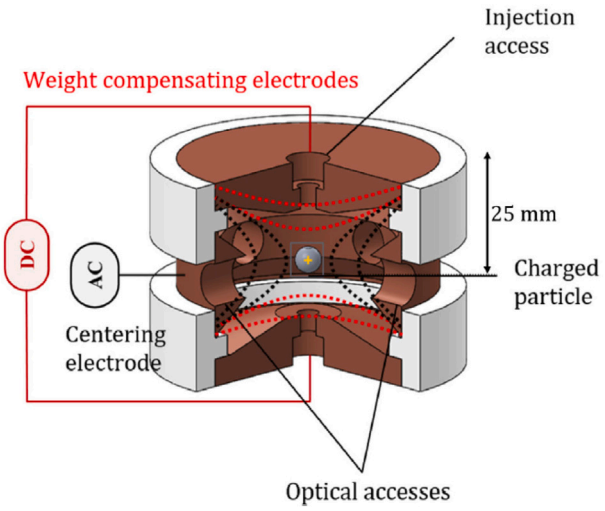

Fig. 2. Schematic of the electrodynamic levitator adapted with permission from [38]. Copyright 2021 Elsevier. For clarity, the particle is depicted larger than its actual size.

The observed phenomena were correlated with the luminosity evolution measured using PM tubes HAMAMATSU THORABS PMT1001. The amount of light received by the PM tubes from the burning particle is regulated manually by adjusting the iris aperture. As the granulometry was similar for all powders (63-106 μm), the iris aperture was kept at 3.5 (on a scale between 0 and 10 which represents respectively a fully closed and a fully open position). This luminance acquisition system is used to ensure that the particle is not overheated while reaching thermal runaway. When the particle reaches a luminance threshold, determined experimentally for each composition (0.5 V, 0.6 V, and 0.7 V respectively for Fe-5Al, Fe-9Al, and Fe-20Al particles), the laser is switched off. Due to a lack of information regarding the calibration coefficients of the PM tubes and their evolution with temperature, one cannot directly transfer the PM signal evolution into a temperature evolution. The overall experimental setup, comprising the electrodynamic levitator, the laser, and the optical diagnostics, is depicted in Fig. 3.

2.3. Multi-particle burner

The manufactured powders are also burned in a multi-particle burner enabling to collect an effective amount of combusted powder to analyze it, which is not possible with the single-particle levitator. The multi-particle burner is composed of three main subsystems: (I) an airflow system, (II) a powder feeding system, and (III) a combustion system (see Fig. 4). The airflow system operates at 1.5 bars to compensate for pressure losses before entering the combustion chamber. The powder feeding system employs a syringe with an inner diameter of 2.2 cm to push metal powder upward into the air stream. The syringe displacement is driven by a piston connected to a stepper motor, allowing precise control of the powder injection rate. The powder-air mixture flows through a set of concentric tubes: first a pilot tube, which reduces the initial

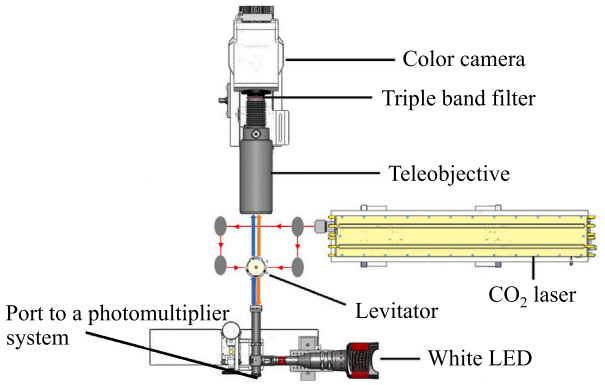

Fig. 3. Schematic of the full experimental setup adapted with permission from [44] including the pathways of the CO_2 laser beam (red arrows), the LED light (blue arrows) and the radiative emissions from the combustion (orange arrows). Copyright 2020 Elsevier.

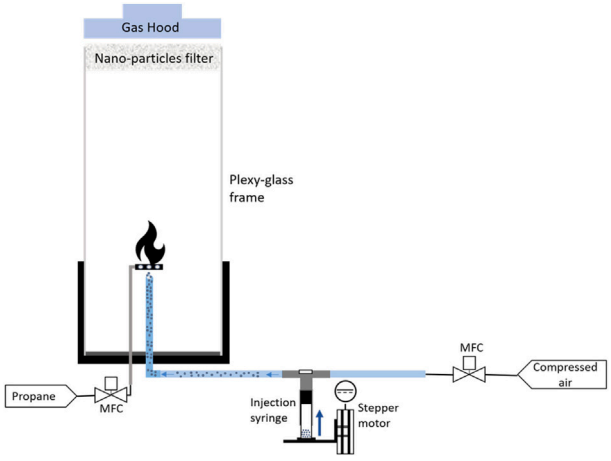

Fig. 4. Schematic of the multi-particle burner.

velocity, followed by a wider tube that minimizes particle agglomeration and wall adhesion. For each combustion test, a single propane flame ring was used as the combustion flame. No separate secondary fuel stream is used and the propane flame is ignited externally, which allowed to stabilize it before powder injection. A plexiglass enclosure was then positioned to cover the reaction zone. The propane flow rate was set to 100 L/h, regulated by a mass flow controller (Brooks 5850S, 0–400 ln/h CO, 4–20 mA). Once a steady flame was reached, metallic powder (45–63 μm) was injected at a feeding rate of 0.05 g/s into the flame region, where particle ignition occurred. The air flow rate used was 5.8 Nm^3/h. For each composition, a total of 3 g of powder was burned (60 s of feeding). A co-flow system surrounds the outlet tube to stabilize the flame and protect the reaction zone from external disturbances. The entire combustion system is enclosed in a plexiglass box for safe observation of the flame. A nanoparticle filter is installed at the top, just below a gas hood, to capture nano-sized combustion products before removing the gases created during the combustion. Micron-sized particles generated by the metal combustion process are collected in a recovery tray at the base.

3. Results

This section starts with the presentation of the different *in situ* observations made using the single-particle levitator. The number of successfully burned particles for each composition is 25, 18, and 16 respectively for Fe-5Al, Fe-9Al, and Fe-20Al powder. In the following, we start by detailing the three consecutive steps observed during the combustion of Fe-5Al particles: (I) Melting and lobe formation, (II) Surface oxidation, and (III) Surface covering. A fourth section is dedicated to the observations of the gas phase. Then, similarities and differences between Fe-5Al and Fe-9Al or Fe-20Al particles are highlighted. Finally, the last section contains the *ex situ* microstructural analysis conducted on the collected combustion products from the multi-particle burner.

3.1. Single-particle combustion of Fe-5Al particles

3.1.1. Particle melting and lobe formation

Upon laser ignition, the surface of all 25 burned Fe-5Al particles is divided into two distinct phases. Once laser is shut down, the first snapshots recorded by the high-speed color camera capture the melting of the external layer (see Fig. 5 for an 80 μm Fe-5Al particle). Thereafter, the initially homogeneous surface divides into two liquid phases with one brighter than the other, due to a different surface emissivity between them, as the temperature is considered homogeneous within the droplet. Regarding the higher emissivity of the oxide phase, the brighter phase initially covering the whole particle surface is an oxide phase while the darker phase is metallic. Therefore, the combustion starts with the melting of the native oxide layer. The molten oxide phase then gradually migrates across the particle surface and accumulates at a single location, ultimately forming a distinct lobe. The time required for complete melting and lobe formation is typically on the order of 1 ms (the lower and upper bounds observed are respectively 0.16 ms and 1.6 ms), though it can vary depending on factors such as particle size, position within the laser beam, and the thickness of the native oxide layer.

3.1.2. Surface oxidation and luminosity evolution

Following lobe formation, discrete bright circular spots begin to nucleate on the exposed metallic surface of the droplet (see Fig. 6). Initially, these spots appear randomly across the metallic region and vary in size (between 1 and 10 μm diameter). Their similar luminosity to the lobe suggests that they are constituted of the same oxide phase. In addition, once formed, they migrate toward the lobe, contributing to its growth. This early stage transition into a more organized oxidation regime: the emerging circular oxide zones appear homogeneously across the whole metallic region and now have the same initial size. This initial size increases with time (from around 1 μm diameter to around 10 μm diameter in 2 ms). They still move synchronously toward the lobe. Eventually, this coordinated oxidation pattern dissipates, and the formation of new oxide regions slows and reverts to a more random and irregular behavior, as illustrated in the last snapshots of Fig. 6 with the oxide spots having different diameters and not covering the whole metallic region.

After laser heating, Fe-5Al particles exhibit a multi-peak luminosity profile during combustion (see Fig. 7). As illustrated in Fig. 7, the multi-peak region arises from the spinning of the particle which takes place for all particles: The PM tubes detect periodic changes as the metallic (darker) and oxide (brighter) sides alternate in view. It is important to note that the PM tubes and the high-speed camera observe opposite sides of the particle at any given time, which accounts for the temporal mismatch between visible surface changes and recorded luminosity drops. A pronounced luminosity drop occurs at the end of the multi-peak, below the lowest level reached during the multi-peak. At the same time, the luminosity of the metallic phase gets significantly darker, suggesting that the oxidation process slows down significantly and eventually ceases. The luminosity then rises again to a similar level as before the drop and the particle gets fully covered by the brighter phase. Subsequently, it plateaus and then rises steadily to the peak (see Fig. 7). Close to the peak, the luminosity often features a sharp increase associated with a sudden inflation event, an effect previously reported in earlier work [9,45]. The particle then enters a cooling phase, with the luminosity declining until a final solidification jump, consistent with observations in pure iron combustion [45]. For 4 Fe-5Al particles out of 18 successfully burned, no bigger luminosity drop occurs at the end of the multi-peak.

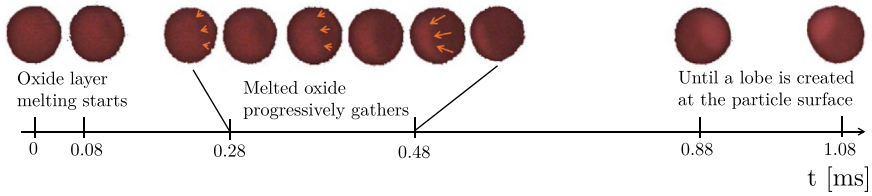

Fig. 5. Snapshots recorded by the high-speed color camera after laser heating for a 80 µm Fe-5Al particle. Once the melting of the external oxide layer starts, the melted oxide phase gathers to form a lobe. (For interpretation of the references to colour in this figure legend, the reader is referred to the web version of this article.)

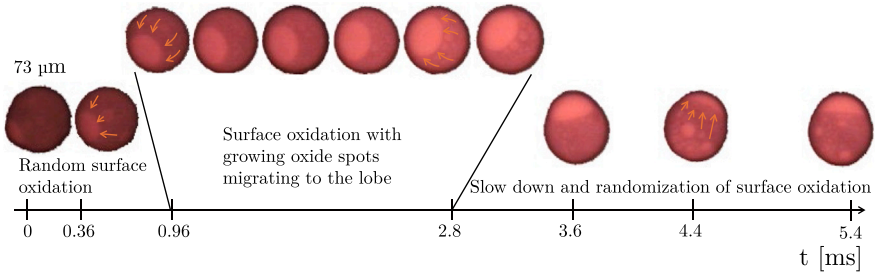

Fig. 6. *In situ* high-speed imaging of the liquid-state combustion of a 73 µm Fe-5Al particle. After lobe formation, oxide spots appear at the surface of the droplet in the metallic region. They first appear at random locations and with a random size between 1 and 10 µm, followed by a consistent surface oxidation pattern both for their initial size and location. After a few ms, this organized pattern of oxidation goes back to the initial random surface oxidation.

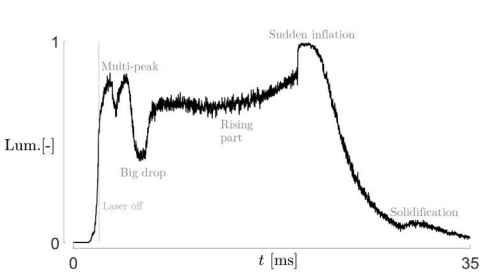

(a) After laser heating, the ignited particle features a multi-peak evolution followed by a bigger luminosity drop. Then, it goes back to its previous level before the drop, plateaus and rises to the peak, followed by a decrease during cooling until solidification.

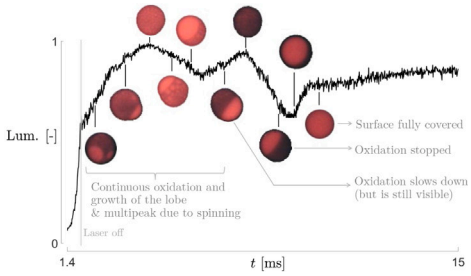

(b) The multi-peak profile is due to the spinning of the particle. A bigger luminosity drop occurs at the end of the multi-peak when surface oxidation over the metallic region slows down and ends.

Fig. 7. Luminosity evolution measured by the PM tubes during the combustion of a 52 µm (a) and 70 µm (b) Fe-5Al particle. For (b), it is correlated with the snapshots recorded by the high-speed color camera. (For interpretation of the references to colour in this figure legend, the reader is referred to the web version of this article.)

The variations are only due to the spinning of the particle. In these cases, oxidation continues over the metallic surface until the lobe envelops the entire particle surface, marking the onset of the steady luminosity rise.

3.1.3. Surface covering

The mechanism by which the droplet surface becomes fully covered differs depending on whether surface oxidation over the metallic region has stopped or not. When it does not stop, the lobe gets big enough to expand and cover the whole particle surface. However, when it is not the case and surface oxidation slows down and eventually stops, a second oxide lobe begins to form and gradually spreads across the remaining metallic surface (see Fig. 8). During this process, the initial lobe remains unchanged, and the metallic region serves as an interface between the two lobes. Once the entire metallic area is covered by the newly formed oxide, the two lobes merge into a single structure. Interestingly, as illustrated in Fig. 8(b), during the formation of the second lobe, a specific case with a distinct bright circular spot surrounded by metallic phase is observed within the new lobe. Rather than contributing to the growth of the new lobe, the latter moves to let the new spot migrate toward the original lobe, resembling the earlier oxidation behavior seen prior to the formation of the second lobe. This means that the created oxide spot can enter into solubility with the first lobe, but not with the second one, suggesting that the two lobes differ in composition. Out of the 25 burned particles, the full covering by the first lobe was observed for 7 particles, the second lobe creation and merging was also observed for 7 particles, and the 11 other particles left the camera's field of view before surface covering.

3.1.4. Gas phase

Once the oxide lobe is formed, a visible gas-phase cone appears around it (see Fig. 9(a)). This cone remains aligned with the lobe as the droplet spins, even during ongoing surface oxidation across the metallic region. Nevertheless, this cone is only clearly visible for 6 particles out of the 25 tests. Similar to observations in pure aluminum particle combustion, the cone is attributed to the condensation of evaporated species around the lobe [32,34]. Additionally, when surface oxidation ceases and a second lobe begins to form (see Section 3.1.3), a distinct gas-phase trail emerges. It represents the visible path created by the gaseous species. This trail follows the remaining metallic region and gradually vanishes as the newly formed lobe fully envelops the droplet surface (see Fig. 9(b)).

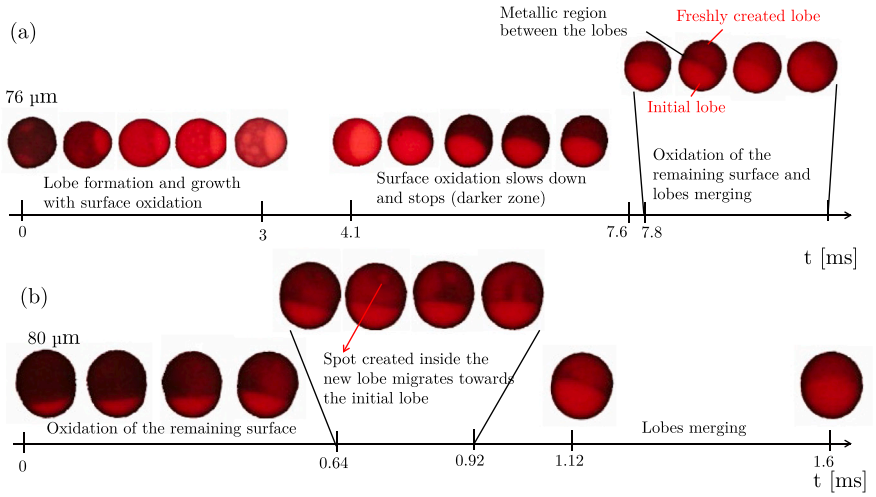

Fig. 8. *In situ* high-speed imaging showing the lobe formation, growth, and covering of the whole surface of (a) a 76 µm and (b) the specific covering of a 80 µm Fe-5Al particle. When surface oxidation over the metallic region slows down and stops, indicated by the surface darkening, a second lobe is created and progressively covers the whole metallic region. The two lobes finally merge together. Particle (b) shows a particular case suggesting that the composition of the two lobes is different: During the formation and covering of the second lobe, an oxide spot surrounded by the metallic phase is created and migrates from the new lobe towards the initial one.

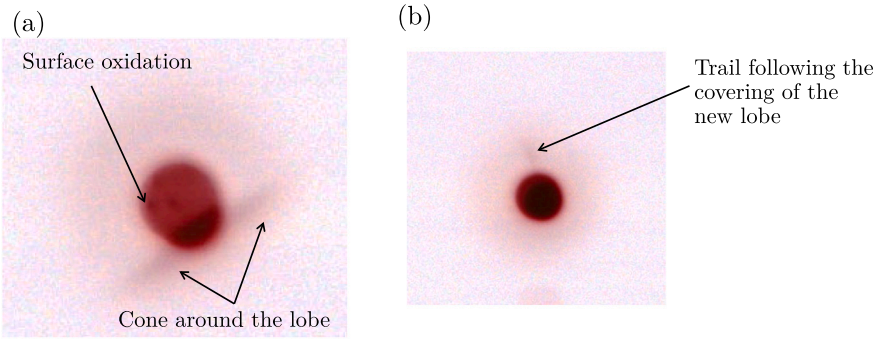

Fig. 9. Snapshots recorded by the high-speed color camera during the combustion of a 84 µm Fe-5Al particle. The colors have been inverted compared to the previous snapshots presented up to now to allow visualization of the gas phase. (a) A cone is visible in the gas phase around the lobe. (b) When the second lobe is created and covers the droplet surface, a trail formed in the gas phase is following the position of the metallic region. (For interpretation of the references to colour in this figure legend, the reader is referred to the web version of this article.)

3.2. Single-particle combustion of Fe-9Al particles

All Fe-9Al particles exhibit a combustion behavior that initially resembles that of Fe-5Al particles: The native oxide layer melts and aggregates into a lobe, followed by the onset of random surface oxidation across the metallic region (see Fig. 10). However, shortly after lobe formation and the beginning of surface oxidation, Fe-9Al particles rapidly develop a jetting motion, propelling themselves in the direction of the lobe. This phenomenon was not observed for Fe-5Al particles, but it concerns all burned Fe-9Al particles. Surface oxidation continues during jetting, but the rapid displacement of the particle out of the camera's field of view complicates detailed combustion analysis. Despite this, the luminosity profiles recorded by the PM tubes remain similar to those of Fe-5Al particles (see Fig. 10), suggesting that jetting does not hinder effective combustion. Additionally, the gas-phase cone surrounding the initial lobe is again visible (for 11 cases out of 18, not including the cases where jetting occurred early and might have prevented a clear observation of the gas phase) and is even more pronounced than for Fe-5Al particles.

3.3. Single-particle combustion of Fe-20Al particles

As with the other powders, combustion of all Fe-20Al particles begins with the melting of the native oxide layer and the formation of a distinct lobe. While random surface oxidation initiates briefly, it ceases within less than 1 ms. As shown in Fig. 11, the metallic region remains smooth and homogeneous, with no observable oxide spots. Instead, the particles undergo sustained spinning for several milliseconds, resulting in an extended multi-peak region in the luminosity profile (see Fig. 12). Concurrently, a gas-phase cloud develops around all particles during lobe formation and gradually evolves into a well-defined cone (see Fig. 11). Although this phenomenon is consistent with observations in Fe-5Al and Fe-9Al particles, the cloud and resulting cone are significantly more prominent and easier to observe in Fe-20Al particles. After the multi-peak, luminosity drops like for Fe-5Al and Fe-9Al particles, but the luminosity level stays low and luminosity steadily decreases (see Fig. 12).

In most instances, Fe-20Al particles exit the camera's field of view while still spinning and without any further surface oxidation. However,

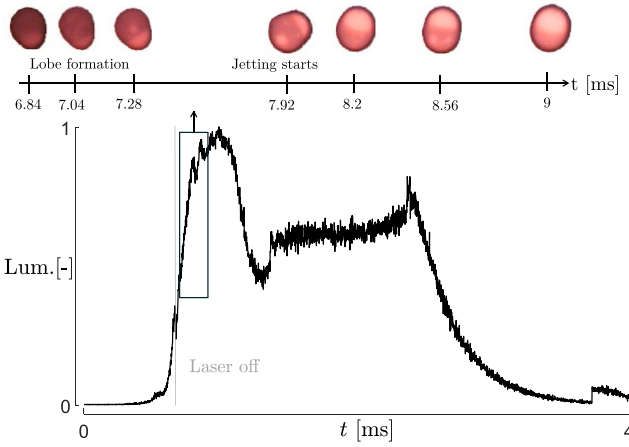

Fig. 10. *In situ* high-speed imaging and luminosity evolution of a 50 µm Fe-9Al particle. Lobe formation is similar to that of Fe-5Al particles, but the particle rapidly features a jetting motion that move it out of the recording scope. Yet, the luminosity evolution is similar to that of Fe-5Al particles.

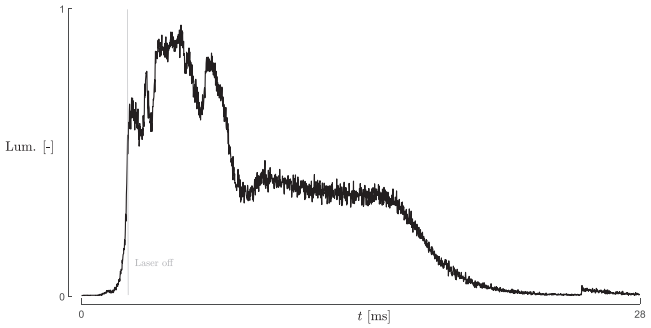

Fig. 12. Luminosity evolution of a 48 µm Fe-20Al particle measured with the PM tubes. Associated to its longer spinning, the luminosity evolution presents a longer multi-peak region. After it, luminosity drops and then decreases, preventing to reach a peak.

in certain cases, surface oxidation resumes while the particle remains observable. As shown in Fig. 13, when oxidation restarts on the metallic region, the particle abruptly stops spinning and transitions into a jetting motion, consistently directed toward the lobe. This behavior mirrors that observed in Fe-9Al particles.

3.4. Ex situ microstructural and chemical characterization

Fe-5Al, Fe-9Al, and Fe-20Al powders were combusted in the multi-particle open-flame burner, collected, and subsequently analyzed *ex situ*. Unlike the single-particle levitation experiments, where the laser ensured sufficient thermal input for ignition, the latter was not guaranteed in the open propane burner for all injected particles. Yet, it offers the possibility to collect and analyze the combusted powders.

3.4.1. Combustion efficiency

The x-ray diffraction (XRD) patterns of the collected Fe-5Al, Fe-9Al, and Fe-20Al powders before and after combustion in the multi-particle open-flame burner are presented in Fig. 14. Only α-Fe was identified in the initial Fe-5Al and Fe-9Al alloyed powders. Concerning initial Fe-20Al particles, they are constituted of both α-Fe and FeAl intermetallic phases. The combustion efficiency is defined as one minus the percentage of alpha-Fe phase, considering that once ignited, the particle reaches the liquid state and all the metal liquid gets oxidized to an oxide liquid; while non-ignited particles are mostly constituted of pure metal. Repeated XRD analysis for Fe-Al powder gives a Fe_3O_4 content of 86.5 ± 2.1 wt.% (mean ± SD) with the remaining fraction corresponding to α-Fe, suggesting that ignition was largely successful and yielding a combustion efficiency of 86.5%. In contrast, Fe-9Al powder exhibited very limited ignition; their diffraction patterns were dominated by metallic α-Fe (> 99 wt.%), with only trace amounts of Fe_3O_4 (< 1 wt.%). For Fe-20Al particles, no peaks associated with a Fe_3O_4 phase were detected, confirming the limited ignition (combustion efficiency < 1%). Yet, as later presented in Section 3.4.3, a few ignited Fe-20Al particles could be observed by SEM. Therefore, the quantity of oxide phase in the combusted sample of Fe-20Al powder is likely too small to be detected by XRD. For all powders, no Al-based crystalline phases were detected. As shown by the local chemical analyses by SEM-EDS (see Figs. 15–17), Al is mostly present in solid solution in the Fe-rich phases, i.e., alpha-Fe and Fe_3O_4. Al-rich oxide phases are also observed locally, e.g., in Al-rich oxide lobes, but the latter were not detected by XRD because of their low quantity, under the detection threshold of XRD (~ 1 vol.%). In addition to the XRD analysis which only quantifies the proportion of crystalline phases, and not the oxygen content of the combustion powders, the latter was analyzed using an O/N/H analyzer (LECO ONH836) but led to underestimated oxygen content as discussed in Supplementary Information SI4.

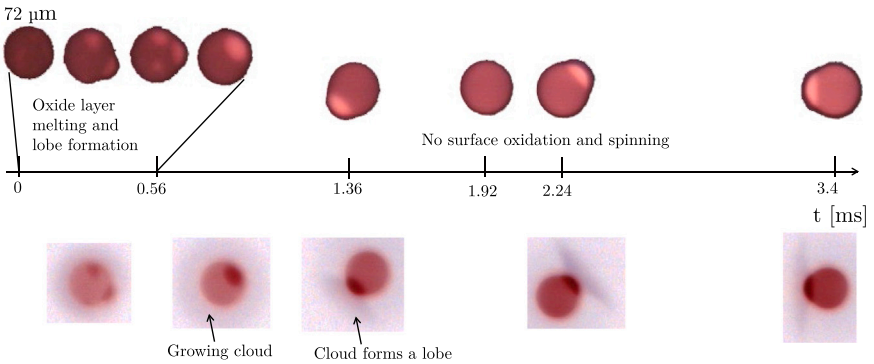

Fig. 11. *In situ* high-speed imaging of a 72 µm Fe-20Al particle. Bottom snapshots are with inverted colors to highlight the gas phase. Fe-20Al particles first feature a similar lobe formation as Fe-5Al particles. However, surface oxidation over the metallic region does not take place and the particle rather spins. A gas cone is present around the lobe and follows it during spinning. (For interpretation of the references to colour in this figure legend, the reader is referred to the web version of this article.)

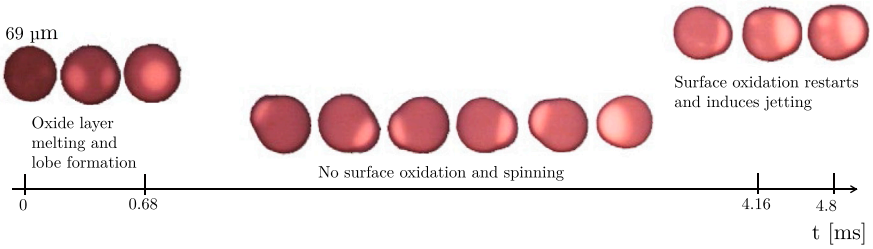

Fig. 13. *In situ* high-speed imaging of a 66 µm Fe-20Al particle. Fe-20Al particles stop spinning when surface oxidation starts: Oxide spots appear at the surface and migrate towards the lobe. From that moment, the droplet stops spinning and jets in the direction of the lobe.

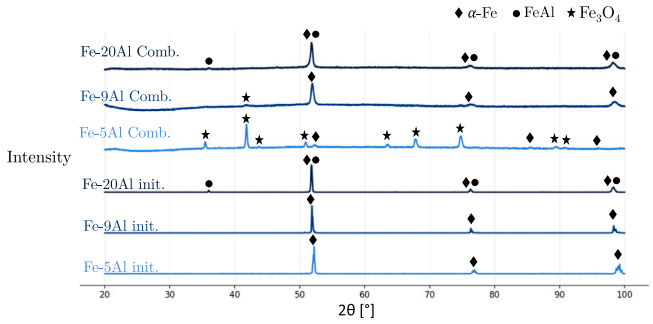

Fig. 14. XRD curves of both initial and combusted Fe-Al powders. For the combusted powders, they show a major presence of metallic α-Fe phase in Fe-9Al and Fe-20Al powders ($>$ 99%), and a larger proportion of Fe_3O_4 phase in the Fe-5Al powder (88%), with remaining 12% α-Fe phase. Since Al is not detected in the initial powders, it is probably present in solid solution in α-Fe and Fe_3O_4 phases for both initial and combusted powders.

3.4.2. Solid-state oxidation

Cross-sectional SEM analysis of particles that failed to ignite (see Fig. 15) revealed an Al-rich outer oxide shell for all Fe-Al compositions. After this external layer, there exists another intermediate oxide layer, richer in Al compared to the external one, surrounding the metallic core. For all powders, both external layers were identified as a complex Fe-Al oxide. Nevertheless, the difference in Al content between these two layers increases with the initial Al content: respectively 3.5 wt.%, 7.6 wt.%, and 16.1 wt.% for the Fe-5Al, Fe-9Al, and Fe-20Al particles presented in Fig. 15. For all particles, the Al concentration in the metallic core is lower than the initial Al content.

3.4.3. Ignited particles

Unlike the majority of collected particles (ignited or not) that stay spherical (see Supplementary information SI5), a few collected particles present a different morphology with a lobe (see Fig. 16), similar to the observations made during the combustion of laser-ignited particles (see Fig. 6). It is assumed that the particles presenting a lobe result from quenching before the end of their combustion process. The lobe is constituted of a complex Fe-Al oxide, with an increasing proportion of Al with the initial Al content from 23.9 wt.% for the Fe-5Al particle to 61.9 wt.% for the Fe-20Al particle. The remaining particle surface is constituted of a Fe-rich oxide for Fe-5Al and Fe-9Al particles, and of a metallic phase similar to the initial composition stained with a few oxide spots (up to 6 wt.% O) for the Fe-20Al particle. These oxide spots are consistent with the surface oxidation pattern constituted of oxide zones created randomly over the particle surface (see Fig. 11).

3.4.4. Fully combusted particles

As suggested by the XRD pattern of combusted Fe-5Al powder (see Fig. 14), successfully ignited Fe-5Al particles displayed a homogeneous magnetite phase containing Al in solid solution (see Fig. 17(a). Despite the overall low combustion efficiency ($<$ 1%), a few fully combusted Fe-9Al and Fe-20Al particles were also observed (see Fig. 17(b)-(c)). The latter exhibit dendritic solidification microstructures, with Al-rich and Fe-rich dendrites. Such morphologies are characteristic of solidification from a multi-component liquid, demonstrating that these particles reached the liquid state prior to cooling. An external iron oxide layer surrounding these particles was also observed. It may form either due

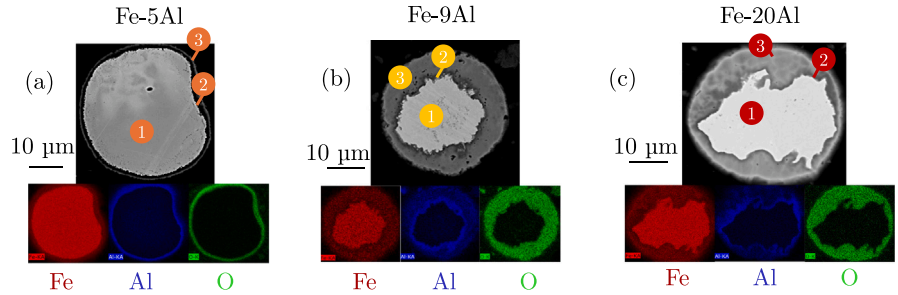

[wt.%]	Fe	Al	O
1	93.8	6.1	0.1
2	64.3	16.5	19.2
3	62.2	13	24.8

[wt.%]	Fe	Al	O
1	92.4	5.4	2.1
2	54.3	20.8	24.9
3	52.4	13.2	34.4

[wt.%]	Fe	Al	O
1	95.2	4.8	0
2	52	27.3	20.7
3	70.8	11.2	18

Fig. 15. SEM-EDS analysis of the cross-section of not ignited (a) Fe-5Al, (b) Fe-9Al, and (c) Fe-20Al particles collected from the multi-particle open propane flame burner. Not ignited particles show an Al-rich outer oxide layer. The latter is followed by an intermediate layer, even richer in Al, surrounding the metallic core.

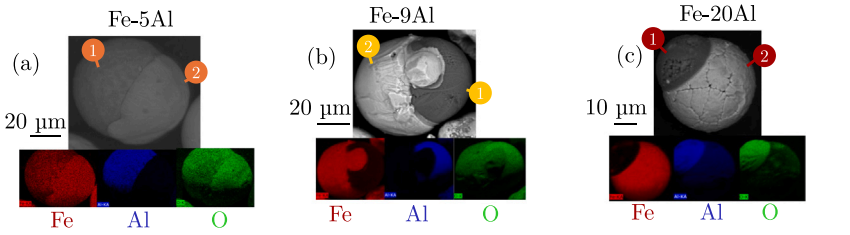

[wt.%]	Fe	Al	O
1	49.5	23.9	26.6
2	79.9	1.3	18.8

[wt.%]	Fe	Al	O
1	14.4	53	32.6
2	86.2	3	10.8

[wt.%]	Fe	Al	O
1	4.4	61.9	33.7
2	69.5	27.3	3.2

Fig. 16. SEM-EDS analysis of the surface of quenched (a) Fe-5Al, (b) Fe-9Al, and (c) Fe-20Al particles collected from the multi-particle open propane flame burner. They showed the presence of a complex Fe-Al oxide lobe, with an increasing Al fraction with the initial Al content. The remaining particle surface is constituted of a Fe-rich oxide for Fe-5Al and Fe-9Al particles, and of a metallic phase similar to the initial composition stained with a few oxide spots for the Fe-20Al particle.

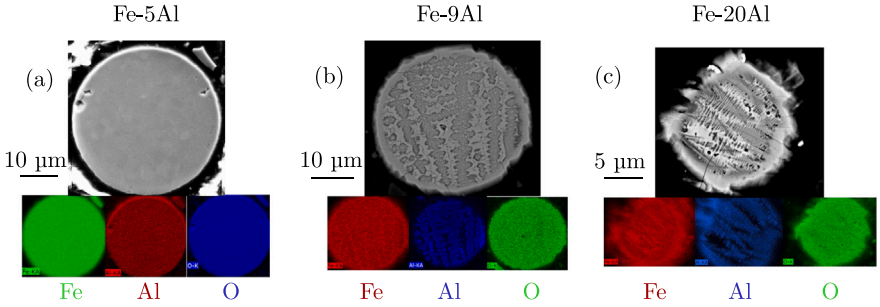

Fig. 17. SEM-EDS analysis of the cross-section of ignited (a) Fe-5Al, (b) Fe-9Al, and (c) Fe-20Al particles collected from the multi-particle open propane flame burner. Ignited Fe-5Al particles feature an homogeneous distribution of Fe and Al, while Fe-9Al and Fe-20Al combusted particles are constituted of Fe-rich and Al-rich dendrites.

to a subsequent solid-state oxidation, which would create a hematite phase (Fe_2O_3), present in too low quantity to be detected by XRD, or from initial solidification between Fe-rich and Al-rich oxides.

4. Discussion

Based on both the *in situ* and *ex situ* analysis, we propose that Fe-Al alloyed particles follow the combustion mechanism described in Fig. 18. The different steps are roughly described in this section, followed by a more detailed discussion about the solid-state oxidation and ignition in Section 4.1, the subsequent liquid-state combustion in Section 4.2, and the evaporation dynamics in Section 4.3.

Before ignition, an Al-rich oxide layer is created at the particle surface due to the higher affinity of Al with O. This layer mitigates the combustion efficiency of the alloyed powder by slowing down internal ions diffusion and subsequently the oxidation rate, which increases the ignition temperature required to reach thermal runaway. If the ignition threshold is reached, the particle melts and the initial oxide phase gathers into a lobe due to surface tension-driven flow and differences in wettability. After its formation, the lobe is supplied with oxide spots created over the remaining surface and migrating to it to maintain the thermodynamically predicted immiscibility between oxide and metallic liquid phases (see thermodynamic simulations in Supplementary information SI6). At the same time, evaporation of both Fe and Al takes place from the metallic region of the surface, even if the boiling temperature is not reached like for pure Fe particles. The evaporated species oxidize in the gas phase and either migrate and condense at the lobe

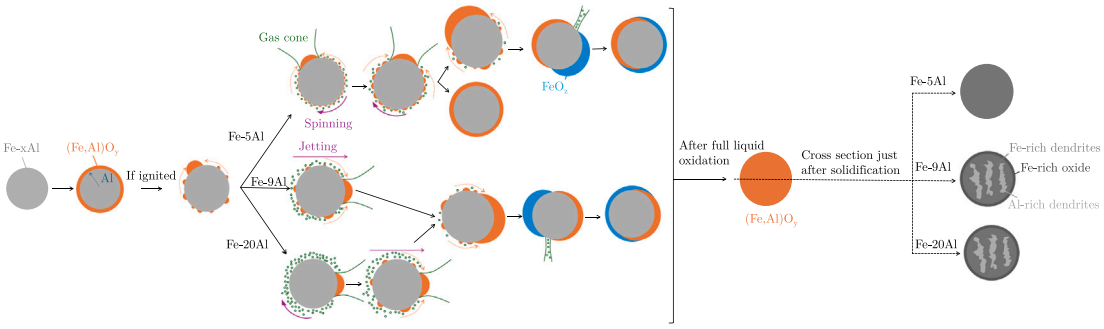

Fig. 18. Proposed combustion mechanism of Fe-Al alloyed particles. The same color is used for the phases containing the same components even when their relative proportion may vary. (For interpretation of the references to colour in this figure legend, the reader is referred to the web version of this article.)

creating a gas cone around it, or move away from the burning particle. As no evaporation takes place from the lobe, the asymmetry involves spinning and jetting motions of the particle.

Fe-5Al particles first follow a coordinated oxidation pattern where oxide zones of the same size homogeneously emerge and migrate to the lobe. Their size increases with time until the lobe becomes sufficiently big to completely cover the particle surface. If the lobe is not big enough, the surface oxidation pattern continues but becomes random (in terms of location and size of the oxide spots) and then stops. Thereafter, an iron oxide phase progressively covers the remaining metallic surface to create a dual lobe configuration, due to a different Al content between the two lobes. The progressive concentration of the gaseous species over the decreasing metallic surface eventually leads to a visible gas trail.

Combustion of Fe-9Al and Fe-20Al particles is similar but due to the increased Al content, more evaporation takes place, accentuating the jetting/spinning motions. Fe-9Al particles present similar random oxidation pattern to Fe-5Al particles and rapidly feature jetting. After lobe formation, Fe-20Al particles burn in a gaseous combustion regime similar to pure Al particles, followed by a random surface oxidation pattern leading to jetting. The following combustion pattern is similar to that of Fe-5Al particles with the dual lobe structure.

All particles that completely oxidize in the liquid state are constituted of a single oxidized liquid phase, with compositional variations. During solidification, Fe-5Al particles create a homogeneous magnetite phase with Al in solid solution, while Fe-9Al and Fe-20Al particles create Al-rich and Fe-rich dendrites.

One limitation of this work is the presence of Mo inside the initial powders. It is thermodynamically expected to fully evaporate after melting (see Supplementary information SI6), with a limited impact on particle temperature (< 5K for 5 wt.% Mo in pure Fe particles [3]). While we observed similar combustion time and *in situ* visualization between pure Fe particles and Fe-3Mo particles in our previous work [35], no comparison could be made to justify that Mo has no impact on the combustion of Fe-Al alloys. Nevertheless, regarding that none of the phenomena observed for Fe-Al alloyed particles (lobe creation, jetting and spinning motions, gas cone, etc.) were observed in our previous study for Fe-3Mo particles, we believe that they can be attributed to the presence of Al. Yet, this statement must be treated carefully as the heterogeneity in Mo content between particles may influence the wettability of the liquid phases, and its partial evaporation (predicted by the thermodynamic simulations presented in Supplementary information SI6) may hinder the first lobe covering. Similar powders composition without Mo should be produced and tested to confirm this hypothesis.

4.1. Solid-state oxidation and ignition

In the open propane flame burner, the presence of 9 wt.% and 20 wt.% aluminum significantly hinders particle ignition (combustion efficiency < 1%), whereas most Fe-5Al particles successfully ignite and oxidize to magnetite (combustion efficiency of 86.5%). Prior studies on Fe-Al steel alloys have demonstrated that Al enhances oxidation resistance by forming a protective Al_2O_3 layer which reduces the diffusivity of both Fe and O ions [46–48]. Due to its higher oxygen affinity, Al preferentially oxidizes during the initial stages of combustion, as also predicted thermodynamically (see thermodynamic simulations presented in Supplementary information SI6), by diffusing toward the particle surface. This is supported by the observation of the decreased Al content in the metallic core compared to the external oxide layers, despite the homogeneous initial composition. According to previous studies [49,50], the composition of the resulting oxide layer varies with initial Al concentration: from sequential layers of Fe_2O_3, Fe_3O_4, and $FeAl_2O_4$, respectively from the surface to the core, below 0.5 wt.% Al to a $FeAl_2O_4$ outer layer with an underlying Al_2O_3 sub-layer when the Al content increases to 1–3 wt.%. The last sub-layer is suggested to strongly inhibit iron cations diffusion, and subsequently oxidation. This is consistent with our observation that the difference in Al content between the intermediate and external Al-rich complex oxide increases with the initial Al content. Therefore, we believe that these Al-rich layers prevent proper ignition of Fe-Al particles.

At lower Al concentrations (< 5 wt.%), the successful ignition observed in this study indicates that the thermal energy brought by the burner was sufficient to overcome the presence of Al-rich layers and sustain ignition. However, at higher Al contents, the thicker Al-rich layers act as an effective diffusion barrier, suppressing further oxidation and thereby preventing ignition. While the formation of such oxide layers is beneficial for corrosion resistance in alloyed steels, it poses a significant drawback for the ignition of micron-sized Fe-Al particles.

It should be noted that the burner used in this study was not optimized for particle ignition, and that the Al compositional threshold may vary with the energy brought for ignition. Apart from laser heating which heats the particles while limiting oxidation, the formation of an Al-rich oxide layer is inevitable in the open-flame burner because oxidation takes place and Al has a higher affinity with O than Fe. Nevertheless, regarding that some Fe-9Al and Fe-20Al particles still successfully ignited, the burner itself also impacts the combustion efficiency, which could be improved by testing other burner designs and operating conditions. For example, the decreased oxidation rate could be compensated with a longer residence time at high temperature by decreasing the injected powder mass flow rate and increasing the propane flame length. Therefore, further studies should concentrate on the best conditions and burner designs for the ignition of Fe-Al powders, the main parameter governing its heat release efficiency.

The Al compositional threshold above which ignition is hardly reached (using the multi-particle burner and operating conditions of this study) is also influenced by the statistical distribution of the Al content inside each batch (see Supplementary Information SI2). In particular, while the distribution of the chemical composition overlaps in part between batches Fe-5Al (10th percentile = 2.8 wt.%; 90th percentile = 7.2 wt.%) and Fe-9Al (10th percentile = 5.1 wt.%; 90th percentile = 12.2 wt.%), the ignition efficiency goes from 86.5% for the Fe-5Al powder to < 1% for Fe-9Al powder. For the presented multi-particle burner and experimental conditions, the threshold in Al content to ensure ignition is thus between 5.1 wt.% and 12.2 wt.%. Similarly, as the threshold might be close to the Al content of some particles from the Fe-5Al batch, the non-ignition of some particles in that batch might be due to their higher local Al content. Accordingly, the achieved combustion efficiency of 86.5% could be improved by narrowing the distribution to the median of 5.1 wt.%.

Although ignition is the main difficulty to extract heat from Fe-Al alloyed particles with a high Al content, ignited particles still reach a full liquid-state oxidation. This is particularly interesting to increase the specific heat release regarding the higher specific heat enthalpy of Al compared to Fe (31.1 MJ/kg when oxidizing to Al_2O_3 compared to 6.7 MJ/kg for Fe oxidizing to Fe_3O_4). In the current multi-particle burner, the heat release of Fe-5Al particles, oxidizing to 86.5 wt.% Fe_3O_4 leading to a heat release of 7.5 MJ/kg, is even bigger than that of pure Fe particles burned using the same multi-particle burner, oxidizing to 93 wt.% Fe_3O_4 + 2 wt.% Fe_2O_3 + 1 wt.% FeO [8] and leading to a heat release of 6.5 MJ/kg. The use of Fe-Al alloys as metal fuel is therefore an interesting candidate for energy storage, at the intermediate between Fe and Al fuels.

4.2. Liquid-state combustion

After ignition, the melted oxide phase at the surface gathers into a distinct and immiscible lobe. This behavior is attributed to surface tension-driven flow and differences in wettability between the oxide and metallic phases. This immiscibility between the metallic and oxide liquid phases is also predicted thermodynamically, and simultaneous oxidation of both Fe and Al from the metallic liquid phase is expected (see thermodynamic simulations in Supplementary information SI6). Accordingly, once the lobe is formed, oxide spots start appearing over

the particle surface and migrate toward the lobe. This surface oxidation continues either until the lobe expands to fully cover the droplet or until the oxidation slows down and stops, followed by the formation of a second lobe with a different composition. This dual-lobe structure is also observed in quenched particles (see Fig. 16), which likely results from rapid cooling events, such as ejection of the burning particles from the flame during combustion. For Fe-5Al and Fe-9Al particles, the associated EDS maps revealed that one lobe comprises a complex ternary oxide containing both Fe and Al, while the other is predominantly iron oxide. The structure observed for the quenched Fe-9Al particle in Fig. 16(b) suggests a similar lobe covering as for Fe-5Al particles. Furthermore, the Al content inside the complex ternary oxide lobe increases with the initial Al content. The Fe-20Al particle also presents a complex ternary Fe-Al oxide lobe, with a high proportion of Al, but the remaining surface is overall metallic with partial zones being oxidized. Therefore, this suggests that this particle was quenched during an early stage of the combustion, explaining the low oxidation level of the surface which was still oxidizing according to the pattern described in Fig. 6. Nevertheless, regarding the similar dendritic structure of combusted particles between Fe-9Al and Fe-20Al particles, the latter are also expected to feature a similar dual lobe covering.

The fact that two lobe covering paths are possible for Fe-5Al particles (see Section 3.1.3) cannot be attributed to the particles size as no clear trend emerges between particles featuring a complete covering by the first lobe from the others. This is rather attributed to a different particle temperature reached after laser ignition, affecting the oxidation rate and therefore the growth rate of the lobe. Depending on the exact position of the levitating particle inside the laser beam, it may receive a different heat supply rate, leading to a different particle temperature [35]. No more information about the lobe covering can be gained from Fe-9Al and Fe-20Al particles as they rapidly left the camera's field of view due to their jetting motions.

Based on these compositional differences, we infer that the initial lobe consists of a complex Fe-Al oxide, consistent with the early presence of Al at the surface and its higher oxygen affinity. The remainder of the droplet surface is a metallic phase containing both Fe and Al. If all Al has been oxidized, oxidation of both Fe and Al transitions to only Fe oxidation, resulting in the formation of the second, iron-rich lobe. The persistence of a metallic surface during this phase is supported by the visible gas cloud surrounding it, indicative of enhanced evaporation relative to oxide regions. A gas-phase trail, observed as this surface is subsequently covered by the iron oxide lobe, further confirms this interpretation. The similar emissivity of the two lobes does not allow to determine which one ultimately dominates the droplet surface after merging. Nevertheless, the configuration observed in Fig. 16(b) suggests that the iron oxide lobe progressively covers the other lobe. In any case, when fully oxidized, the liquids are merged into one liquid phase of homogeneous composition, as suggested by the microstructure observed in the fully combusted particles (see Fig. 17). This implies that the two distinct lobes merge and chemically homogenize before liquid oxidation is complete, forming a single complex ternary oxide phase before solidification. The mechanism and driving force for the formation of two lobes could be the minimization of the interfacial and surface energy. Once surface oxidation of the metallic region of the particle surface ends and stops making the first lobe grow, the other lobe rapidly appears and covers the remaining surface as a consequence of surface energy minimization, i.e., governed by the wettability of the lobes on the liquid metal. Still, one unique liquid oxide phase is thermodynamically favored in the Fe-Al-O system, driving the two lobes to merge together.

The microstructure of the solidified, fully combusted Fe-5Al particles and Fe-9Al/Fe-20Al particles can be interpreted on the basis of their thermodynamic simulations (detailed in Supplementary information SI6). When solidification of the ternary liquid oxide phase starts, Al shows a higher tendency to solidify at the beginning of magnetite formation than Fe. Physically, it translates into an Al-enrichment in the first solid formed, in the center of the magnetite dendrites, while a depletion in Al can be expected at the end of solidification, in the boundaries of the magnetite dendrites. This Al-enrichment is stronger as the Al content increases. For Fe-5Al particles, a homogeneous Al distribution is observed, while a separation between Al-rich and Fe-rich oxides is obtained for Fe-9Al and Fe-20Al particles. For Fe-5Al particles, the Al content of the oxide liquid phase is low enough so that it stays in solid solution inside the formed magnetite.

The direct reduction rate of the combusted Fe-Al powders is expected to decrease with the Al content [7]. During the reduction process, only Fe will be reduced, while Al will stay oxidized. While Fe_3O_4 will be reduced to FeO (or directly to Fe, depending on the reduction temperature), Al will stabilize the magnetite phase, and eventually form $FeAl_2O_4$. Increasing amount of Al will increase the relative stability of magnetite and amount of $FeAl_2O_4$, slowing down the reduction process. However, for small Al content, as in Fe-5Al, the formation of a few $FeAl_2O_4$ can form micro-cracks, enhancing gas diffusion [51]. In the case of Fe-9Al and Fe-20Al, the chemical separation between Al-rich and Fe-rich oxides within the dendrites could be beneficial for the reduction process, offering preferential paths for the reduction of Fe in the connected Fe-rich oxide zones.

4.3. Evaporation dynamics

Evaporation plays a more prominent role in the combustion of Fe-Al powders than in pure iron particles, as evidenced by (I) the appearance of a gaseous cone surrounding the lobe and (II) spinning and jetting behaviors. Drawing parallels with aluminum combustion, we propose that the gaseous species evaporate from the metallic surface, undergo gas-phase oxidation, and their oxides subsequently condense at the lobe. The tendency of each element ($Fe_{(g)}$ and $Al_{(g)}$) to evaporate depending on the temperature and the metallic phase composition has been computed using thermodynamic equilibrium calculations (see Supplementary information SI7). This method does not include the evaporation kinetics and the results should then be carefully interpreted. Nevertheless, they show that both gaseous species are expected to evaporate, to a different extent depending on the composition of the metallic phase and the temperature. $Fe_{(g)}$ is thermodynamically favored compared to $Al_{(g)}$ for Fe-5Al and Fe-9Al due to the higher Fe concentration in the metallic phase, while $Al_{(g)}$ becomes favored for Fe-20Al. Consequently, both elements are expected to evaporate. Due to the low combustion efficiency (< 1%) of Fe-9Al and Fe-20Al powders, which featured the strongest evaporation rate as observed from single-particle experiments, the amount of nanoparticles produced in the multi-particle burner was too low to successfully collect and analyze them. Further characterization of collected nanoparticles from a burner ensuring a better combustion efficiency should be conducted to better identify the most evaporating species.

A second key indicator of enhanced evaporation dynamics is the spinning and jetting behavior observed. These motions are driven by Stefan flow, namely a gas displacement at the liquid–gas interface caused by evaporation. Since evaporation is suppressed at the oxide lobe, the resulting flow is asymmetric, producing a net force that propels the particle (jetting) and a torque that induces rotation (spinning) [33]. The earlier onset of jetting in Fe-9Al particles, compared to Fe-5Al, suggests that a higher aluminum content leads to more intense evaporation and thus more pronounced asymmetry in mass flux. Furthermore, the cone becomes increasingly pronounced with higher Al content (see Fig. 11). This cone corresponds to an interface of lower temperature between the gas-phase reaction zone and the cold region at the lobe. The condensation of alumina nanoparticles is thus largely promoted at this cold interface. Additionally, the jetting behavior is amplified by surface oxidation and the migration of oxide spots toward the lobe. This coupling is clearly illustrated in Fe-20Al particles: After lobe formation, they initially spin but do not jet until surface oxidation resumes. The higher evaporation with Al content can be explained on one side by the higher Al concentration in the metallic phase (see Supplementary information

SI7), and on the other side, by the increase in the particle temperature due to the higher specific enthalpy of Al. A dedicated characterization of the PM calibration coefficients with temperature would be required to measure it and is left for further improvement. Yet, although the particle temperature was not monitored, thermodynamic simulations presented in Supplementary information SI6 predict an increase in flame temperature with the Al content: 2396 K, 2546 K, and 2815 K for Fe-5Al, Fe-9Al, and Fe-20Al, respectively. This higher particle temperature could explain the delay in oxidation onset observed for Fe-20Al particles as well as their strictly decreasing luminosity profile after the multi-peak. If a higher temperature is reached due to the higher presence of Al, the particle can reach a gas diffusion combustion regime similar to pure Al particles. In that case, evaporation occurs across the whole metallic particle surface, the particle spins, and no surface oxidation takes place (see Fig. 13). When surface oxidation resumes, potentially due to a decrease in particle temperature, the particle jets as explained before. Accordingly, the second part of luminosity profile of Fe-20Al particles following the multi-peak is at a much lower luminosity level (see Fig. 12) compared to Fe-5Al and Fe-9Al particles for which luminosity increases back to a similar level as during the multi-peak (see Figs. 7 and 10).

5. Conclusion

The combined approach using both a single-particle and multi-particle burner gave us critical insights into the combustion behavior of Fe-Al alloy particles containing 5, 9, and 20 wt.% Al.

First, the formation of an Al-rich oxide layer during the heating phase inhibits ignition in powders with the two highest Al contents. This imposes a constraint on the allowable aluminum content in iron-based powders intended for use in the MeCRE. In contrast, Fe-5Al particles ignited more readily, and their combustion products consisted primarily of magnetite. This indicates that the presence of Al does not prevent the system from reaching the highest liquid-state oxidation level. However, the current experimental setup does not allow the solidified particles to remain in a hot gas environment long enough to undergo potential solid-state oxidation. Further experiments using alternative burners are recommended to explore the potential of these powders in terms of combustion efficiency.

Second, although the iron mass loss due to evaporation was not quantified in this study, qualitative visual observations from single-particle experiments suggest that the presence of aluminum leads to increased evaporation compared to pure iron. Moreover, given the liquid-phase configuration with a metallic surface, the evaporation rate is likely higher than in pure Fe combustion. Therefore, evaporation should be controlled to minimize iron losses and nanoparticle formation.

Finally, achieving full circularity for these powders requires the reduction of the combustion products. The higher oxygen affinity of Al may enable selective reduction of iron oxides while maintaining aluminum in its oxidized form. However, the presence of Al dissolved in the magnetite phase could complicate reduction kinetics [3,7]. Experimental reduction studies are required to evaluate the circularity of the combusted Fe-Al powders.

Beyond the specific findings for Fe-Al alloys, this study underscores the broader impact that alloying elements can have on the combustion regime of iron-based particles. Given the wide range of possible alloying elements or impurities present in iron feedstocks, this work encourages the metal-fuels research community to expand their focus to include a broader range of powder compositions.

CRediT authorship contribution statement

Z. Bruyr: Writing – original draft, Visualization, Software, Resources, Methodology, Investigation, Funding acquisition, Conceptualization. **L. Ahmad:** Writing – review & editing, Visualization, Resources, Methodology, Investigation. **L. Choisez:** Writing – review & editing, Supervision, Resources, Investigation, Conceptualization. **F. Halter:** Writing – review & editing, Supervision, Resources, Conceptualization. **F. Contino:** Writing – review & editing, Supervision, Resources, Funding acquisition, Conceptualization.

Declaration of competing interests

The authors declare the following financial interests/personal relationships that may be considered as potential competing interests:

Zakarie Bruyr reports that financial support was provided by Fund for Scientific Research. Laurine Choisez reports that financial support was provided by Fund for Scientific Research. If there are other authors, they declare that they have no known competing financial interests or personal relationships that could have appeared to influence the work reported in this paper.

Acknowledgements

The authors acknowledge Hugo Keck for his help with the manipulation of the single-particle experimental setup and the important discussions about the combustion mechanism of pure Al particles. This work has received funding from the Fonds De La Recherche Scientifique - FNRS. ZB acknowledges financial support through F.R.S.-FNRS doctoral mandate. LC acknowledges financial support through F.R.S.-FNRS chargée de recherche mandate (ID40011141).

Appendix A. Supplementary data

EDS maps of initial particles, statistical analysis of particles chemical composition inside each initial powder, XPS measurements of the chemical composition of particles surface, SEM image of combusted sample of Fe-5Al powder, oxygen content measurement for combusted powders (ONH analysis), thermodynamic simulations of Fe-Al alloys adiabatic combustion, activity of gaseous Fe and Al in equilibrium with liquid metallic Fe-5Al, Fe-9Al, and Fe-20Al phases, recorded videos of the single-particle combustion of one Fe-5Al, Fe-9Al, and Fe-20Al particle.

Supplementary data to this article can be found online at doi:10.1016/j.fuel.2026.139083.

Data availability

Data will be made available on request.

References

[1] Bergthorson JM, Goroshin S, Soo MJ, Julien P, Palecka J, Frost DL, Jarvis DJ. Direct combustion of recyclable metal fuels for zero-carbon heat and power. Appl Energy 2015. 160:368–82.[Online]. Available: https://www.sciencedirect.com/science/article/pii/S0306261915011071.

[2] Bergthorson JM. Recyclable metal fuels for clean and compact zero-carbon power. Prog Energy Combust Sci 2018. 68:169–96.[Online]. Available: https://www.sciencedirect.com/science/article/pii/S0360128518300327.

[3] Choisez L, Van Ende M-A, Bruyr Z, Contino F, Jacques PJ. Influence of impurities on the use of fe-based powder as sustainable fuel. Philos Trans R Soc A Math Phys Eng Sci 2024. 382(2284):20230236. [Online]. Available: https://royalsocietypublishing.org/doi/abs/10.1098/rsta.2023.0236.

[4] Peng F, Kong C, Liu H, Mi X, Xu S, Liu Y, Cai W. Ignition and combustion of a single iron particle with impurities in hot post-flame gas flow. Combust Flame 2024. 265:113509. [Online]. Available: https://www.sciencedirect.com/science/article/pii/S0010218024002177.

[5] Choisez L, Stevens N, Prasidha W, Kuypers B, Mauxion T, de Goey P, Finotello G, Jacques PJ. On the use of industrial steel mill scale as a high-density energy carrier: Part i. reaction processes and particle size evolution over cycling. Fuel 2026. 405:136614. [Online]. Available: https://www.sciencedirect.com/science/article/pii/S0016236125023397.

[6] Choisez L, Kuypers B, Stevens N, Prasidha W, Mauxion T, de Goey P, Finotello G, Jacques PJ. On the use of industrial steel mill scale as a high-density energy carrier: Part ii. microstructural and chemical evolution over cycling. Fuel 2026. 406:136906. [Online]. Available: https://www.sciencedirect.com/science/article/pii/S0016236125026316.

[7] Bruyr Z, Choisez L, Thijs LC, Mi XC, Jacques PJ, Halter F, Contino F. Combustion of a single iron-based impure particle: numerical analysis of four non-volatile oxide impurities using a parametric approach. Fuel 2026. 407:137277.[Online]. Available: https://www.sciencedirect.com/science/article/pii/S0016236125030029.

[8] Ahmad L, Contino F, Jacques PJ, Choisez L. On the pore formation during combustion of direct reduced iron powders. 2025, manuscript submitted for publication.

[9] Bruyr Z, Choisez L, Ahmad L, Eloy P, Halter F, Contino F. Influence of chemical additions and specific surface area on micro-explosion of burning iron particles.

Energy Fuels 2026. [Online]. Available: 40(6):3382–96. https://doi.org/10.1021/acs.energyfuels.5c05699
[10] Peng F, Liu H, Kong C, Mi XC, Tian B, Zheng Y, Xu S, Cai W. Micro-explosion of burning iron particles with carbon impurity. Combust Flame 2025. [Online]. Available: https://api.semanticscholar.org/CorpusID:275730437.
[11] Mi X, Fujinawa A, Bergthorson JM. A quantitative analysis of the ignition characteristics of fine iron particles. Combust Flame 2022. 240:112011. [Online]. Available: https://www.sciencedirect.com/science/article/pii/S001021802200030X.
[12] Ning D, Shoshin Y, van Stiphout M, van Oijen J, Finotello G, de Goey P. Temperature and phase transitions of laser-ignited single iron particle. Combust Flame 2022.236:111801. [Online]. Available: https://www.sciencedirect.com/science/article/pii/S0010218021005447.
[13] Panahi A, Chang D, Schiemann M, Fujinawa A, Mi X, Bergthorson JM, Levendis YA. Combustion behavior of single iron particles–part i: an experimental study in a drop-tube furnace under high heating rates and high temperatures. Appl Energy Combust Sci 2022. 100097. [Online]. Available: https://www.sciencedirect.com/science/article/pii/S2666352X22000401.
[14] Hameete J, Abdallah MS, Thijs LC, Homan TAM, Mi XC, Dam NJ, de Goey LPH. Particle-resolved hyperspectral pyrometry of metal particles. Combustion Flame 2024. 264:113435. [Online]. Available: https://www.sciencedirect.com/science/article/pii/S0010218024001445.
[15] Prasidha W, Baigmohammadi M, Shoshin Y, de Goey P. Towards an efficient metal energy carrier for zero–emission heating and power: Iron powder combustion. Combust Flame 2024. 268:113655. [Online]. Available: https://www.sciencedirect.com/science/article/pii/S001021802400364X.
[16] Wiinikka H, Vikström T, Wennebro J, Toth P, Sepman A. Pulverized sponge iron, a zero-carbon and clean substitute for fossil coal in energy applications. Energy & Fuels Aug 2018;32.
[17] Chang D, Thijs LC, Panahi A, Mi X, Bergthorson JM, Levendis YA. Effects of oxygen concentration on nanoparticle formation during combustion of iron powders. Fuel 2025. 397:135366. [Online]. Available: https://www.sciencedirect.com/science/article/pii/S0016236125010919.
[18] Thijs LC, Kritikos EM, Giusti A, Ramaekers G, van Oijen JA, de Goey P, Mi X. On the surface chemisorption of oxidizing fine iron particles: insights gained from molecular dynamics simulations. Combust Flame 2023. 254:112871.[Online]. Available: https://www.sciencedirect.com/science/article/pii/S0010218023002523.
[19] Thijs LC, Van Ende M-A, van Oijen JA, de Goey P, Mi X. A numerical study of internal transport in oxidizing liquid core–shell iron particles. Combustion Flame 2025. 271:113826. [Online]. Available: https://www.sciencedirect.com/science/article/pii/S0010218024005352.
[20] Fujinawa A, Thijs LC, Jean-Philyppe J, Panahi A, Chang D, Schiemann M, Levendis YA, Bergthorson JM, Mi X. Combustion behavior of single iron particles, part ii: a theoretical analysis based on a zero-dimensional model. Appl Energy Combust Sci 2023. 14:100145. [Online]. Available: https://www.sciencedirect.com/science/article/pii/S2666352X23000341.
[21] Mich J, da Silva AK, Ning D, Li T, Raabe D, Böhm B, Dreizler A, Hasse C, Scholtissek A. Modeling the oxidation of iron microparticles during the reactive cooling phase. Proc Combust Inst 2024.40(1):105538. [Online]. Available: https://www.sciencedirect.com/science/article/pii/S1540748924003468.
[22] Zou X, Wang N, Han L, Xue R, Xu C, Zhuang W, Shi B. Investigation on burning behaviors of aluminum agglomerates in solid rocket motor with detailed combustion model. Acta Astronaut 2023. 206:243–56. [Online]. Available: https://www.sciencedirect.com/science/article/pii/S0094576523000796.
[23] Emelyanov VN, Teterina IV, Volkov KN. Dynamics and combustion of single aluminium agglomerate in solid propellant environment. Acta Astronaut 2020. 176:682–94.[Online]. Available:https://www.sciencedirect.com/science/article/pii/S0094576520301740.
[24] Joslin DL, Easton DS, Liu CT, David SA. Reaction synthesis of feal alloys. Mater Sci Eng A 1995, 3rd International Conference on High Temperature Intermetallics. 192-193:544–8. [Online]. Available: https://www.sciencedirect.com/science/article/pii/0921509394032726.
[25] Kou Y, Wang Y, Zhang J, Guo KG, Song XL. Iron/aluminum nanocomposites prepared by one-step reduction method and their effects on thermal decomposition of ap and an. Defence Technol 2023. 22:74–87.[Online]. Available: https://www.sciencedirect.com/science/article/pii/S2214914721002063.
[26] Sui H, Atashin S, Wen JZ. Thermo-chemical and energetic properties of layered nano-thermite composites. Thermochim Acta 2016. 642:17–24. [Online]. Available: https://www.sciencedirect.com/science/article/pii/S0040603116302222.
[27] Glassman I, Yetter RA, Glumac NG. Combustion. Academic Press; 2014.
[28] Beckstead M. A summary of aluminum combustion. In: RTO/VKI Special Course on Internal Aerodynamics in Solid Rocket Propulsion RTO-EN-023; Jan 2002.
[29] Sundaram DS, Puri P, Yang V. A general theory of ignition and combustion of nano- and micron-sized aluminum particles. Combust Flame 2016.169:94–109. [Online]. Available: https://www.sciencedirect.com/science/article/pii/S0010218016300529.
[30] Yetter RA, Risha GA, Son SF. Metal particle combustion and nanotechnology. Proc Combust Inst 2009. 32(2):1819–38. [Online]. Available: https://www.sciencedirect.com/science/article/pii/S1540748908001715.
[31] Keck H, Chauveau C, Legros G, Gallier S, Halter F. New experimental method for the simultaneous determination of concentration and size profiles of condensed combustion products around a burning aluminum droplet. Combustion Flame 2024. 268:113616.[Online]. Available: https://www.sciencedirect.com/science/article/pii/S0010218024003250.
[32] Dreizin EL. On the mechanism of asymmetric aluminum particle combustion. Combust Flame 1999. 117(4):841–50. [Online]. Available: https://www.sciencedirect.com/science/article/pii/S0010218098001254.
[33] Jüngst N, Wu Z, Ruan C, Aldén M, Li Z. Light extinction and scattering to determine nanoparticle formation rates during droplet jetting in aluminum dust flames. Powder Technol 2025. 453:120633.[Online]. Available: https://www.sciencedirect.com/science/article/pii/S0032591025000282.
[34] Gallier S, Braconnier A, Godfroy F, Halter F, Chauveau C. The role of thermophoresis on aluminum oxide lobe formation. Combust Flame 2021. 228:142–53.[Online]. Available: https://www.sciencedirect.com/science/article/pii/S0010218021000572.
[35] Bruyr Z, Hameete J, Choisez L, Halter F, Contino F. Observation of an unmixed particle surface during single-particle experiments of iron combustion. Fuel 2025. 395:135261. [Online]. Available: https://www.sciencedirect.com/science/article/pii/S001623612500986X.
[36] Braconnier A. Étude expérimentale de la combustion d'une particule d'aluminium isolée: influence de la pression et de la composition de l'atmosphère oxydante, [Ph.D. dissertation], Mechanical Engineering, Université D'Orléans. Oct 2020.
[37] Bar-Ziv E, Sarofim AF. The electrodynamic chamber: A tool for studying high temperature kinetics involving liquid and solid particles. Prog Energy Combust Sci 1991. 17(1):1–65.[Online]. Available: https://www.sciencedirect.com/science/article/pii/0360128591900025.
[38] Braconnier A, Gallier S, Halter F, Chauveau C. Aluminum combustion in co2-co-n2 mixtures. Proc Combust Inst 2021. 38(3):4355–63. [Online]. Available: https://www.sciencedirect.com/science/article/pii/S1540748920300547.
[39] Muller M, El-Rabii H, Fabbro R. Liquid phase combustion of iron in an oxygen atmosphere. J Mater Sci Jan 2015. 50. [Online]. Available: https://doi.org/10.1007/s10853-015-8872-9
[40] Powell CJ. Characteristic energy losses of 8-kev electrons in liquid al, bi, in, ga, hg, and au. Phys Rev Nov 1968. 175:972–82. [Online]. Available: https://link.aps.org/doi/10.1103/PhysRev.175.972.
[41] Huttner B. Optical properties of polyvalent metals in the solid and liquid state: aluminium. J Phys Condens Matter Mar 1994. 6(13):2459. [Online]. Available: https://dx.doi.org/10.1088/0953-8984/6/13/008.
[42] Qiu TQ, Longtin JP, Tien CL. Characteristics of radiation absorption in metallic particles. J Heat Transf May 1995. 117(2):340–5. [Online]. Available: https://doi.org/10.1115/1.2822527
[43] Dombrovsky L. Near-infrared properties of droplets of aluminum oxide melt. Thermopedia Jan 2011. [Online]. Available: https://doi.org/10.1615/thermopedia.000149
[44] Braconnier A, Chauveau C, Halter F, Gallier S. Experimental investigation of the aluminum combustion in different o2 oxidizing mixtures: Effect of the diluent gases. Exp Therm Fluid Sci 2020. 117:110110. [Online]. Available: https://www.sciencedirect.com/science/article/pii/S0894177719320230.
[45] Ning D, Shoshin Y, van Oijen J, Finotello G, de Goey P. Size evolution during laser-ignited single iron particle combustion. Proc Combust Inst 2022. [Online]. Available: https://www.sciencedirect.com/science/article/pii/S1540748922000724.
[46] Roy I, Abouelella H, Rajendran R, Chikhalikar AS, Larsen M, Umretiya R, Hoffman A, Rebak R. Effect of al concentration on fe-17cr alloy during steam oxidation at 400 °c. Corros Sci 2023. 217:111135.[Online]. Available: https://www.sciencedirect.com/science/article/pii/S0010938X23001774.
[47] Prot D, Monty C. Self-diffusion in α-Al_2O_3. ii. oxygen diffusion in 'undoped'single crystals. Philos Mag A 1996. 73(4):899–917.[Online]. Available: https://doi.org/10.1080/01418619608243695
[48] Reddy KPR, Cooper AR. Oxygen diffusion in MgO and alpha-Fe_2O_3. J Am Ceram Soc Jun 2006. 66:664–6.[Online]. Available: https://doi.org/10.1111/j.1151-2916.1983.tb10618.x
[49] Prescott R, Graham MJ. The oxidation of iron-aluminum alloys. Oxid Met 1992. 38(1):73–87. [Online]. Available: https://doi.org/10.1007/BF00665045
[50] Ahmed AHA. Oxidation properties of Fe-Al alloys at 1173k, [Ph.D. dissertation], McMaster University; 1984.
[51] Kapelyushin Y, Xing X, Zhang J, Jeong S, Sasaki Y, Ostrovski O. Effect of alumina on the gaseous reduction of magnetite in co/co2 gas mixtures. Metall Mater Trans B 2015;46(3):1175–85.